Two-Dimensional Materials

Deutsche Ausgabe: DOI: 10.1002/ange.201604784
Internationale Ausgabe: DOI: 10.1002/anie.201604784

Noncovalent Functionalization of Black Phosphorus

*Gonzalo Abellán, Vicent Lloret, Udo Mundloch, Mario Marcia, Christian Neiss, Andreas Görling, Maria Varela, Frank Hauke, and Andreas Hirsch**

Abstract: *Black phosphorus (BP) was functionalized with organic moieties on the basis of liquid exfoliation. The treatment of BP with electron-withdrawing 7,7,8,8-tetracyano-p-quinodimethane (TCNQ) led to electron transfer from BP to the organic dopant. On the other hand, the noncovalent interaction of BP with a perylene diimide was mainly due to van der Waals interactions but also led to considerable stabilization of the BP flakes against oxygen degradation.*

Black phosphorus (BP) has recently emerged as a very interesting two-dimensional material.[1] The individual layers of BP exhibit a honeycomb structure differing from that of graphene because of a marked puckering of the sp^3-hybridized P atoms.[2,3] Due to its intrinsic direct bandgap, a good compromise between charge-carrier mobility and current on/off ratios, and because of its unusual in-plane anisotropy, BP has tremendous potential in both electronics and optoelectronics.[4–9]

Few-layer nanosheets (flakes) of BP can be obtained by mechanical exfoliation of the bulk crystals as well as through solvent exfoliation. However, practical applications are restricted because of the instability of BP with respect to ambient oxygen and moisture.[10–14] Concepts for chemical stabilization are urgently desired. Encapsulation methods have been proposed to preserve the intrinsic properties of BP, but chemical control over its reactivity still remains an open challenge.[3,15,16] Recently, in collaboration with the research group of Coleman, we reported the liquid exfoliation of solvent-stabilized few-layer BP flakes. During this procedure, the stability under ambient conditions increased from approximately 1 h for mechanically cleaved BP to about 200 h for 1-cyclohexyl-2-pyrrolidone (CHP)-exfoliated few-layer BP. The first appealing applications beyond electronics as gas sensors, saturable absorbers, and reinforcing fillers for nanocomposites could be demonstrated.[17] The chemistry of BP, however, remains almost unexplored.[18] So far only single-flake chemistry with diazonium salts and TiL_4 complexes have been reported.[19,20]

We now describe the noncovalent functionalization of bulk BP with 7,7,8,8-tetracyano-*p*-quinodimethane (TCNQ) and a perylene bisimide (PDI) and the resulting pronounced charge-transfer and van der Waals interactions. It was possible to isolate and completely characterize functionalized few-layer BP. The experimental results were supported by quantum-mechanical calculations.

Our chemical approach for noncovalent functionalization involved a combination of pristine BP crystals and TCNQ—an extremely versatile building block for charge-transfer compounds[21]—under inert conditions in an argon-filled glovebox ($O_2 < 0.1$ ppm; $H_2O < 0.1$ ppm; see methods) and gentle magnetic stirring (Scheme 1). The appropriate selection of the solvent has a tremendous influence on the process. We initially anticipated that high-boiling-point solvents, such as NMP and CHP, would form tightly packed solvation shells adjacent to BP surfaces and thus act as a barrier to oxygen/water. However, a screening study with different solvents showed that, surprisingly, TCNQ is able to oxidize some of these systems and create charge-transfer complexes (see Figure S1 and details in the Supporting Information). TCNQ exhibits characteristic absorption spectra in its neutral form (TCNQ), as the aromatized anion radical ($TCNQ^{-}$), and as the dianion ($TCNQ^{2-}$; Figure 1 a,b).[22] The generation of

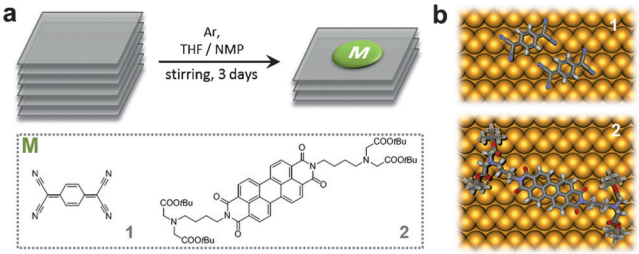

Scheme 1. Functionalization of BP. a) Functionalization of BP without sonication by the use of a strong electron-withdrawing acceptor, TCNQ, and bulk black phosphorous. Charge-transfer compounds consisting of few-layer BP decorated with TCNQ were formed. A second functionalization approach is based on a novel ethylenediaminetetraacetic (EDTA) ligand containing an integral perylene bisimide (PDI) core. b) Schematic representation of TCNQ (top) and PDI molecules (bottom) adsorbed on BP.

[*] Dr. G. Abellán, V. Lloret, U. Mundloch, M. Marcia, Dr. F. Hauke, Prof. A. Hirsch
Department of Chemistry and Pharmacy
Friedrich-Alexander-Universität Erlangen-Nürnberg (FAU)
Henkestrasse 42, 91054 Erlangen (Germany)
and
Joint Institute of Advanced Materials and Processes (ZMP)
Dr.-Mack-Strasse 81, 90762 Fürth (Germany)
E-mail: andreas.hirsch@fau.de
Dr. M. Varela
Universidad Complutense de Madrid
Instituto Pluridisciplinar and Facultad de CC. Físicas
Madrid 28040 (Spain)
Dr. C. Neiss, Prof. A. Görling
Lehrstuhl für Theoretische Chemie
Friedrich-Alexander-Universität Erlangen-Nürnberg (FAU)
Egerlandstrasse 3, 91058 Erlangen (Germany)
Supporting information and the ORCID identification number(s) for the author(s) of this article can be found under http://dx.doi.org/10.1002/anie.201604784.

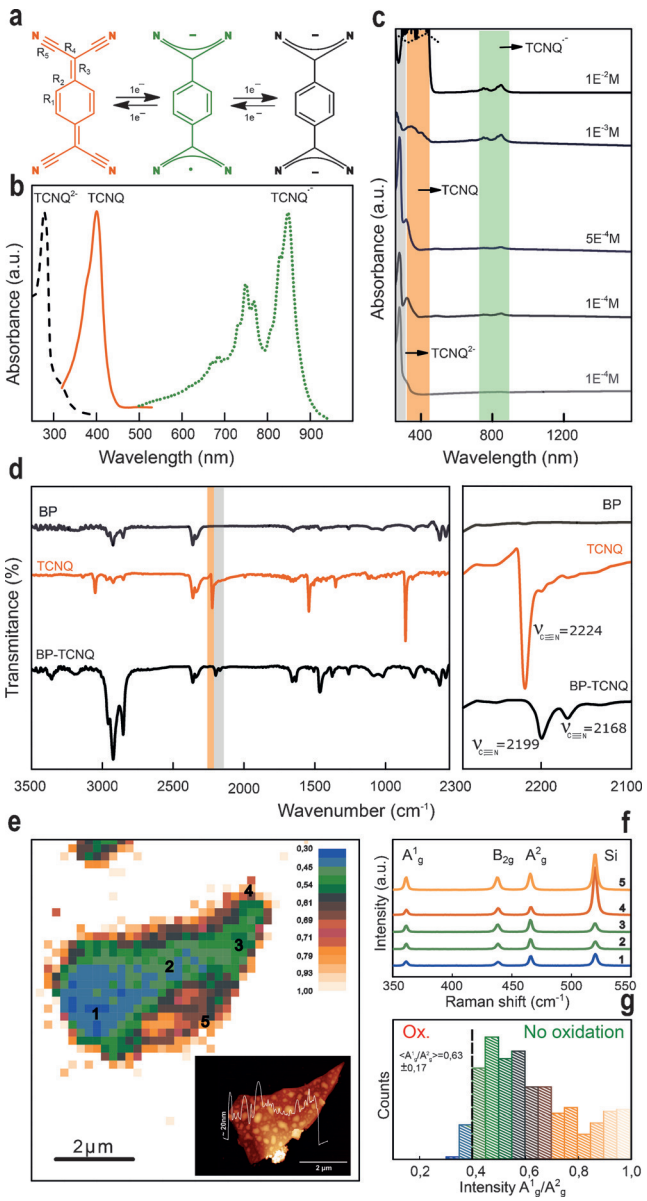

Figure 1. Synthesis and characterization of TCNQ-functionalized BP nanosheets. a) Molecular structure of TCNQ, $TCNQ^{\bullet-}$, and $TCNQ^{2-}$. The TCNQ molecule exhibits a quinonoid structure, with a high single–double bond-length alternancy, whereby R_1 and R_3 are much shorter than R_2.[30] b) Electronic absorption spectra fingerprints of the different TCNQ species in THF solution.[22] The $TCNQ^{\bullet-}$ absorption spectrum was obtained by exhaustive exclusion of O_2 in NMP, and that of $TCNQ^{2-}$ was obtained in the presence of BP (see the Supporting Information). c) Titration experiment with BP highlighting the exclusive formation of BP-TCNQ at concentrations below 10^{-3} M. The typical absorption bands of $TCNQ^{\bullet-}$ and $TCNQ^{2-}$ are indicated as bars. d) ATR-FTIR spectra of pristine BP (gray), TCNQ (orange), and BP-TCNQ (black). e) SRM of a BP-TCNQ (10^{-5} M) flake showing the corresponding A_{1g}/A_{2g} band ratio mapping. f) Mean Raman spectra (excitation at 532 nm) of the areas indicated in (e). g) Histogram of the A_{1g}/A_{2g} intensity ratio. The inset in (e) is an AFM image of the same flake studied by SRM showing an average thickness of 20 nm. The scale bar represents 2 µm.

$TCNQ^{2-}$ requires exhaustive 2 e^- reduction (bulk electrolysis) and the rigorous exclusion of O_2.[22] When we performed the study under extremely inert conditions, several charge-transfer steps between the solvents and TCNQ took place (see Figure S1). Indeed, the spontaneous formation of the mono-anion $TCNQ^{\bullet-}$ took place with *N*-methyl-2-pyrrolidone (NMP) and *N*-cyclohexyl-2-pyrrolidone (CHP), whose spectra revealed the presence of the aromatic form even after the exposure of the solutions to air. It is most likely that the corresponding radical cation of the pyrrolidone is formed during this process. Therefore, the appropriate selection of an inert solvent was required for the development of the redox noncovalent functionalization of BP. For this purpose, THF turned out to be the most appropriate solvent, since it does not react with TCNQ.

For the preparation of the targeted noncovalent hybrids between BP and TCNQ, a mixture of ground BP (ca. 5 mg) in a 10^{-5} M solution of TCNQ in THF (3 mL) was stirred vigorously in the glovebox for a minimum of 3 days, throughout which time the O_2 content was carefully controlled. Indeed, the high quality of the solvent was also reflected in the absence of water absorption peaks in the NIR spectra at around 1430 nm (see Figure S1). Subsequently, a dark colloidal suspension exhibiting the characteristic Faraday–Tyndall effect was obtained. The first clue of success was offered by UV/Vis spectroscopy, which showed the exclusive formation of a species (referred to herein as BP-TCNQ) with a similar UV/Vis spectrum to that of the TCNQ dianion.

In a titration experiment, different TCNQ concentrations ranging from 10^{-5} to 10^{-2} M were tested, while the amount of BP was kept constant (Figure 1c). The amount of $TCNQ^{2-}$ decreased with the concentration, so that a marked shift in the bands was observed at concentrations higher than 10^{-3} M. Free TCNQ only appeared at concentrations greater than or equal to 10^{-3} M; therefore, the optimal working range was 10^{-5}–10^{-4} M, which we then used for the sample preparation and further characterization. Additional evidence for the formation of the charge-transfer complex was provided by attenuated total reflectance FTIR (ATR-FTIR) spectroscopy.

In the ATR-FTIR spectrum of pristine suspensions of BP, TCNQ, and the functionalized BP in THF (Figure 1d), the parent TCNQ exhibited the characteristic vibration frequencies of the cyano group at approximately 2224 cm^{-1}. In stark contrast, the BP-TCNQ complex exhibited a doublet for the cyano group at 2199 and 2168 cm^{-1}, indicative of the formation of $TCNQ^{\bullet-}$, as well as a shoulder at around 2131 cm^{-1}, related to the formation $TCNQ^{2-}$ (see Figure S2). These observations are in accord with those for previously reported samples of $TCNQ^{2-}$-containing coordination polymers,[23–25] and point towards the formation of an anionic TCNQ species on BP under inert conditions, as previously predicted by theoretical calculations.[26–28]

Compound BP-TCNQ was also investigated by scanning Raman microscopy (SRM). Typical results are depicted in Figure 1e–g. We selected different areas with an optical microscope and measured the corresponding spectra with an excitation wavelength of 532 nm (see Figure S3). All spectra showed the characteristic modes of BP, labeled A_g^1, B_{2g}, and

A_g^2. We performed statistical Raman mapping for a selected flake (Figure 1e). We analyzed and plotted the A_g^1/A_g^2 intensity ratio, which gave a well-defined image of the micrometric flake (with an overall thickness of ca. 20 nm, corresponding to less than 35 layers, as subsequently determined by AFM), thus highlighting that there were no areas with $A_g^1/A_g^2 < 0.4$ and confirming the basal planes to be slightly oxidized.[11]

However, significant differences were observed in comparison with CHP-solvent-stabilized few-layer BP, in which $A_g^1/A_g^2 > 0.5$, indicative of a redox reaction with TCNQ as well as degradation by oxygen.[17] Control experiments under inert conditions revealed very similar results (average A_g^1/A_g^2 ratio around 0.6), thus showing slight oxidation in the basal plane (see Figure S4). Consequently, we searched for the characteristic bands of anionic TCNQ. Well-defined ν_3 and ν_4 modes at approximately 1580 and 1329 cm^{-1}, respectively, were encountered at the flake edges, whereas only broad contributions were measured in the basal planes, thus pointing towards a preferential accumulation of TCNQ at the edges (see Figure S4b).[29]

Despite the contributions from residual solvent and adhesion effects, the apparent AFM thickness provides useful information about the exfoliation degree of BP-TCNQ. We relocated under the atomic force microscope the same flake previously studied by SRM (see Figure S3). The inset in Figure 1e shows a typical thickness of approximately 20 nm with lateral dimensions of several microns (see Figure S5).

The characteristic degradation protuberances usually ascribed to the formation of H_3PO_3 and/or H_3PO_4 were also evident in the topographic image (taken after SRM analysis was finished, that is, around 24 h after its first contact with oxygen), thus indicating that interaction with the TCNQ molecules did not prevent the degradation of the flakes (see Figure S4). Thinner flakes were encountered, but they also exhibited smaller lateral dimensions (< 1 micron), thus precluding their use in further statistical Raman analysis (see Figure S5). Our strategy represents a milder alternative to our previously described sonication procedure and yields larger flakes (Figure 1e, inset; see also Figure S5).

To obtain direct microscopic evidence of the noncovalent functionalization of the BP sheets, we analyzed both pristine BP and BP-TCNQ samples by real-space techniques sensitive to both chemistry and structure, such as atomic-resolution aberration-corrected STEM-EELS at 80 kV. Crystal sizes were in the range of microns, as depicted in the low-magnification high-angle annular dark field (HAADF) image in Figure 2a (top left). An atomic-resolution HAADF STEM image of the BP-TCNQ sample acquired down the [110] crystallographic direction with the electron beam perpendicular to the platelet plane is also shown in Figure 2a (right, both raw and Fourier filtered data). The sample is highly crystalline, showing a characteristic puckered structure that appears intact over wide regions of the order of hundreds of nanometers. The lattice shows high uniformity with the presence of very few defects or dislocations. Depending on the zone axis used, the lattice can exhibit a "dumbbell" type configuration. The observed average

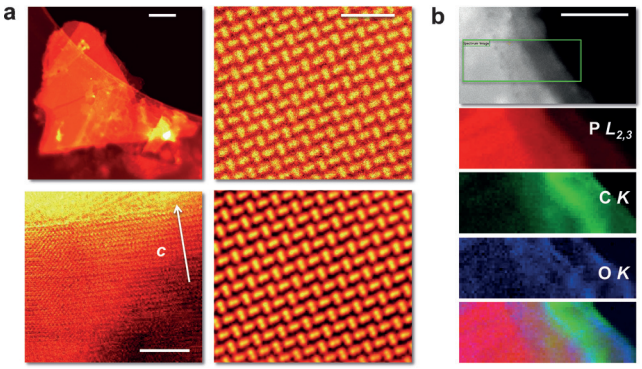

Figure 2. STEM-EELS analysis of BP-TCNQ nanosheets. a) STEM images of a flake (BP-TCNQ, 10^{-5} M). Top left: low-magnification HAADF image (scale bar is 200 nm); bottom left: ABF image of a flake with the *c* axis perpendicular to the electron beam (scale bar is 5 nm); right: atomic-resolution HAADF images down the [110] axis (top: raw data; bottom: Fourier filtered image). All images are in false color; the scale bars for the atomic-resolution images are 1 nm. b) Compositional maps obtained at the edge of a flake. A green rectangle in the HAADF image at the top shows the area for which an EEL spectrum image was acquired. The P, C, and O maps are shown, along with an RGB overlay following the same color scheme. No significant N signal could be detected above the experimental noise. The scale bar represents 50 nm.

thickness (estimated from low-loss EELS measurements) was in the 8–20 nm range, in good accordance with the AFM measurements. Cross-sectional views of the crystals, such as the annular bright-field (ABF) image in Figure 2a (bottom left), show parallel fringes corresponding to interlayer distances of 0.5–0.6 nm, in agreement with previous observations.[31]

To gain additional evidence of functionalization with TCNQ, we also analyzed the chemical composition of the flakes by STEM-EELS. We studied a flake (ca. 10 nm overall thick, corresponding to ca. 15–18 layers) suspended over a hole in order to avoid any contribution from the carbon-coated copper grid. Figure 2b shows the chemical maps obtained from the $L_{2,3}$-edges of P, the C K-edge, and the O K-edge, with onsets near 132, 284, and 532 eV, respectively. These maps, which are more sensitive to the surface molecule coating than HAADF imaging, were produced by subtracting the background by using a power-law fit and then integrating the remaining signal below the edges of interest by using windows with a width of 25 eV. Carbon signals can be observed on all areas, thus pointing to a homogeneous anionic TCNQ surface coverage. Significant accumulation of carbon can be detected on surface steps and flake edges, in agreement with the SRM results. On the other hand, the oxygen mapping reveals a residual contribution mainly located on the edges of the flakes, probably arising from grid transfer into the TEM holder (< 30 s). Control experiments on pristine BP in THF also revealed the absence of carbon, thus ruling out the presence of solvent residues in the basal plane of the flakes. Additionally, EELS mapping showed the predominant presence of oxygen on the edges, terraces with highly degraded rims, amorphous edges, and the presence of holes. These results confirmed the predicted preferential edge degradation of BP (see Figure S6).[17]

To provide clearer experimental evidence of the noncovalent functionalization of BP, we took advantage of the chemical versatility of the family of perylene diimide (PDI)-based molecules. Indeed, our group has used these molecules for the noncovalent functionalization of carbon nanotubes, graphene, and MoS_2. They exhibit a strong absorption due to their large aromatic core, which can become attached to the 2D layers through van der Waals interactions.[32–34] The structure of the selected molecule is depicted in Scheme 1; we used a protected EDTA–PDI molecule to avoid any preferential interaction of the carboxylic moieties (see Figure S7 for synthetic details).[35] Control experiments under strictly inert conditions revealed that NMP can generate highly colored charge-transfer complexes with the PDI molecules, thus exhibiting a dramatic sensitivity against oxygen (Figure 3b; see also Figure S8). This striking result will be fully developed and analyzed in a separate study. The first signature of PDI functionalization was observed by fluorescence spectroscopy (Figure 3c). Upon excitation at 455 nm, the PDI fluorescence emission exhibited dramatic quenching by approximately 66% in the presence of BP, in excellent accordance with previous studies for graphene functionalization (Figure 3c).[33,36] Although perylene diimides exhibit very strong fluorescence—which usually prevents their investigation by Raman spectroscopy—we were able to relocate appropriate flakes by AFM and record a Raman spectrum of the BP-PDI, comprising both the features of BP and PDI, when excited at 532 nm (Figure 3d; see also Figure S9). In the presence of BP, complete quenching of the fluorescence took place, and the characteristic signals of the PDI spectrum were observed (Figure 3e,f; see also Figure S10).

The statistical analysis of Raman spectra by comparison of the Si-normalized intensities of the ν_{A_g} mode of PDI with the A^1_g mode of BP revealed a comparable intensity ratio (Figure 3g; see Figures S11–S13 for additional AFM and Raman analysis). Strikingly, when we analyzed the A_g^1/A_g^2 ratio after 2 days under ambient conditions, we observed an average value of approximately 0.79, similar to that shown by freshly exfoliated flakes and remarkably higher than that exhibited by BP-TCNQ, indicative of non-oxidized samples (see Figure S14). Additionally, we analyzed a substrate after storage for 6 months in a glove box and observed no degradation (see Figure S15). We also analyzed the thermal stability of these flakes after exposure to air by statistical temperature-dependent Raman spectroscopy (see Figure S16).

STEM-EELS analysis (Figure 4) further confirmed the presence of the organic moiety on the surface of the exfoliated crystals, showing flakes within a thickness range of 15–50 nm (estimated from low-loss EELS). Figure 4a (top) shows a low-magnification image of a flake with a size of a few microns. Flakes were crystalline, as shown by atomic-resolution images. Figure 4a (middle) is an intermediate-magnification ABF image showing long-range crystalline order. The inset is a high-magnification HAADF image down the [110] axis. The bottom image in Figure 4a shows a flake with the [001] axis parallel to the electron beam. The interatomic spacing is of the order of 5.5–6.0 Å, and the surface appears coated with an organic layer a few nanometers thick. A study of the chemical composition by EELS is summarized in Figure 4b, in which P (red), C (green), and O (blue) maps are shown from the top to the bottom, along with an RGB superposition of the three. This analysis reveals a complete

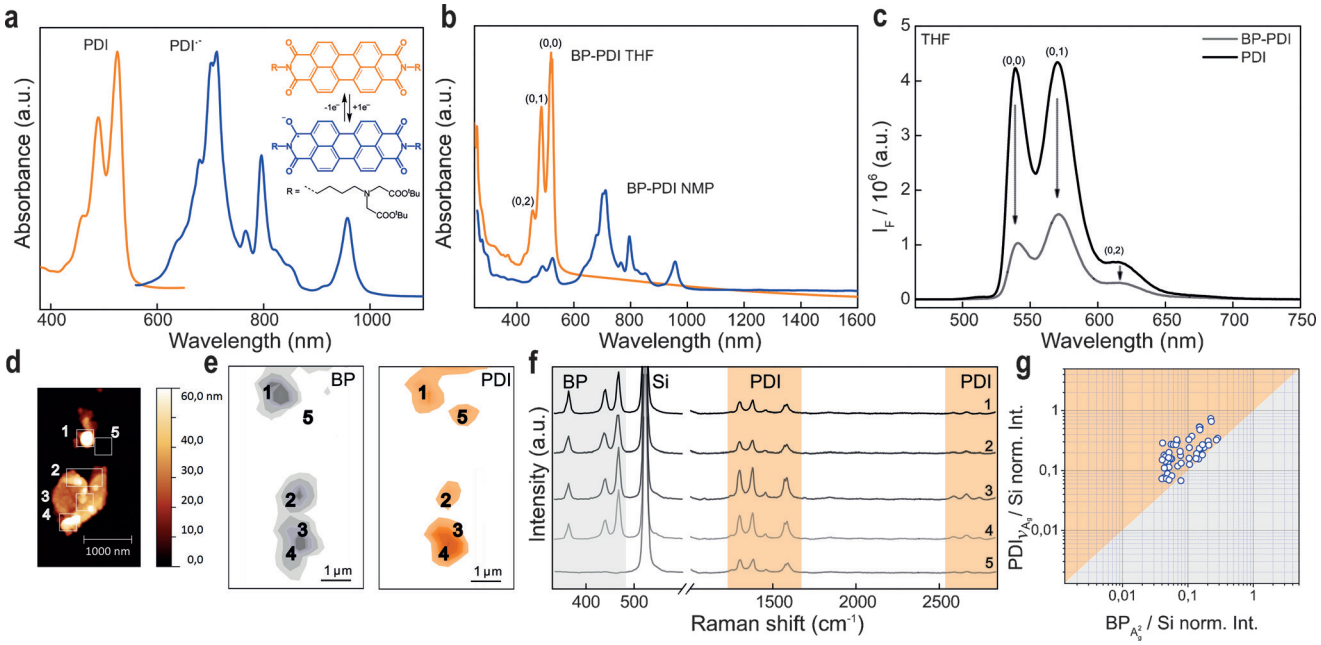

Figure 3. Synthesis and characterization of PDI-functionalized BP nanosheets. a) Molecular structure of the PDI and PDI$^{\bullet-}$. Electronic absorption spectra fingerprints of the different PDI species. b) UV/Vis spectra of BP-PDI in THF and NMP. c) Fluorescence emission spectra of PDI and BP-PDI in THF ($c_{PDI} = 10^{-4}$ M, gray line); $\lambda_{exc} = 455$ nm. d) Representative AFM image and corresponding Raman A^1_g (e, $\lambda_{exc} = 532$ nm) and ν_{A_g} intensity mapping (f) of the same BP-PDI flakes. The numbers denote the areas in which the Raman spectra shown in (f) were recorded. g) Plot of the A^1_g versus ν_{A_g} normalized intensities.

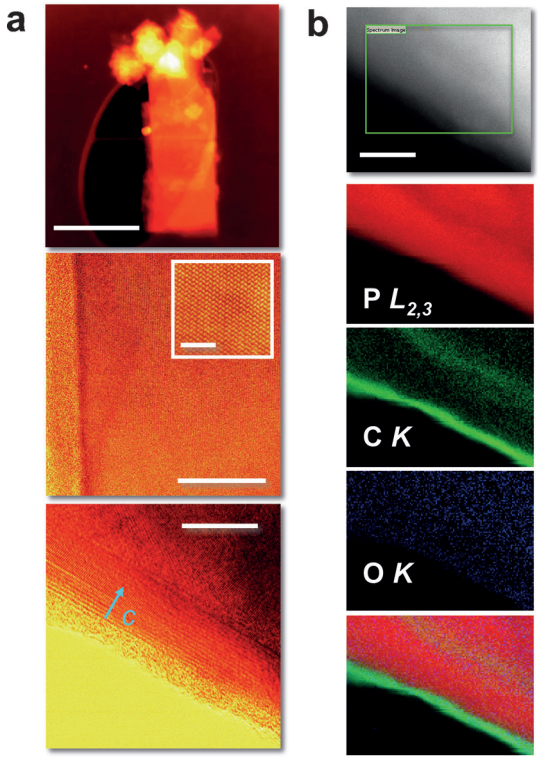

Figure 4. STEM-EELS analysis of BP-PDI nanosheets. a) STEM images of a PDI-coated flake. From top to bottom: low-magnification HAADF image; ABF image of a flake with the [110] axis parallel to the electron beam (inset: atomic-resolution HAADF image down the [110] direction); ABF image of the edge of a flake. All images are in false color; the scale bars, from top to bottom, correspond to 500, 20 (inset: 2 nm), and 10 nm. b) Compositional maps. The green rectangle in the HAADF image at the top shows the area for which an EEL spectrum image was acquired (scale bar: 10 nm). P $L_{2,3}$, C K, and O K maps for this area are shown, along with an RGB overlay following the same color scheme.

coverage of the flakes with C (the PDI moiety); this coverage is more pronounced at the edges. Very little oxygen signal was detected in this sample. Indeed, the measured oxygen counts fall within the experimental noise, as the average O signal detected on the sample was more than a factor of two smaller than the mean square deviation (noise) for the same area or the hole. The low signal level suggests that the PDI protective shell, with a thickness of a few nanometers (3–5 nm visible in the bottom image of Figure 4a), acts as an encapsulation reagent to prevent major environmental degradation of the BP. This effect was corroborated by AFM measurements on single flakes before and after PDI functionalization (see Figure S17 for further information). Further STM experiments to clarify the molecular structure are currently being performed in our laboratory.

Finally, we systematically investigated the supramolecular interaction of TCNQ and PDI on BP by DFT calculations. In the case of TCNQ, the oxidation of the BP flakes was confirmed. Bader population analysis yielded a charge transfer of 0.43 electrons from a single sheet of BP to an adsorbed TCNQ molecule. An increase in the number of BP layers led to a higher degree of electron transfer of 0.65 electrons per TCNQ molecule and was accompanied by an increase in the adsorption energy from 1.3 to 1.6 eV. Owing to the lower reduction potential of PDI, only a weak charge transfer was calculated. See the Supporting Information for further results of the DFT calculations.

In conclusion, we have presented herein a concept for the bulk noncovalent organic functionalization of black phosphorus (BP). The wet-chemical treatment of BP with electron-poor and polarizable polycyclic aromatic compounds, namely, 7,7,8,8-tetracyano-*p*-quinodimethane (TCNQ) molecules and a tailor-made perylene diimide, led to the formation of stable hybrids in which the organic components cover and shield the surface of thin few-layer BP flakes. Experimental and computational studies revealed the nature of the strong noncovalent interaction between these molecules and BP, thus provoking its exfoliation into few layers. In the case of TCNQ, electron transfer from the BP to the organic component takes place. The positive charge on the BP surface is stabilized by the layers underneath, as nicely supported by DFT calculations. Functionalization with the perylene diimide dramatically improved the resistance of the flakes against oxygen degradation. We expect that these initial studies on the fundamental organic chemistry of black phosphorus will provide access to unprecedented 2D materials. The inherent modulation of the physical properties of black phosphorus is likely to lead to a broad range of applications in electronics, optoelectronics, energy storage, sensors, and fillers for composite reinforcement, to name a few.

Acknowledgements

The research leading to these results was partially funded by the European Union Seventh Framework Programme under grant agreement No. 604391 Graphene Flagship. We thank the Deutsche Forschungsgemeinschaft (DFG-SFB 953 "Synthetic Carbon Allotropes", Projects A1 and C2), the Interdisciplinary Center for Molecular Materials (ICMM), and the Graduate School Molecular Science (GSMS) for financial support. Electron microscopy was performed at the Centro Nacional de Microscopia Electrónica (UCM) sponsored by the ERC Starting Investigator Award STEMOX#239739 and Fundación BBVA. G.A. acknowledges the EU for a Marie Curie Fellowship (FP7/2013-IEF-627386).

Keywords: black phosphorus · charge transfer · functionalization · noncovalent interactions · stability

How to cite: *Angew. Chem. Int. Ed.* **2016**, *55*, 14557–14562
Angew. Chem. **2016**, *128*, 14777–14782

[1] A. C. Ferrari et al., *Nanoscale* **2015**, *7*, 4598–4810.
[2] X. Ling, H. Wang, S. Huang, F. Xia, M. S. Dresselhaus, *Proc. Natl. Acad. Sci. USA* **2015**, *112*, 4523–4530.
[3] A. Castellanos-Gomez, *J. Phys. Chem. Lett.* **2015**, *6*, 4280–4291.
[4] J. D. Wood, S. A. Wells, D. Jariwala, K.-S. Chen, E. Cho, V. K. Sangwan, X. Liu, L. J. Lauhon, T. J. Marks, M. C. Hersam, *Nano Lett.* **2014**, *14*, 6964–6970.

[5] A. Castellanos-Gomez, L. Vicarelli, E. Prada, J. O. Island, K. L. Narasimha-Acharya, S. I. Blanter, D. J. Groenendijk, M. Buscema, G. A. Steele, J. V. Alvarez, H. W. Zandbergen, J. J. Palacios, H. S. J. van der Zant, *2D Mater.* **2014**, *1*, 025001.
[6] M. Buscema, D. J. Groenendijk, G. A. Steele, H. S. J. van der Zant, A. Castellanos-Gomez, *Nat. Commun.* **2014**, *5*, 4651.
[7] J. Qiao, X. Kong, Z.-X. Hu, F. Yang, W. Ji, *Nat. Commun.* **2014**, *5*, 4475.
[8] F. Xia, H. Wang, Y. Jia, *Nat. Commun.* **2014**, *5*, 4458.
[9] L. Li, Y. Yu, G. J. Ye, Q. Ge, X. Ou, H. Wu, D. Feng, X. H. Chen, Y. Zhang, *Nat. Nanotechnol.* **2014**, *9*, 372 – 377.
[10] J. Kang, J. D. Wood, S. A. Wells, J.-H. Lee, X. Liu, K.-S. Chen, M. C. Hersam, *ACS Nano* **2015**, *9*, 3596 – 3604.
[11] A. Favron, E. Gaufrès, F. Fossard, A.-L. Phaneuf-L'Heureux, N. Y.-W. Tang, P. L. Lévesque, A. Loiseau, R. Leonelli, S. Francoeur, R. Martel, *Nat. Mater.* **2015**, *14*, 826 – 832.
[12] J. O. Island, G. A. Steele, H. S. J. van der Zant, A. Castellanos-Gomez, *2D Mater.* **2015**, *2*, 011002.
[13] P. Yasaei, B. Kumar, T. Foroozan, C. Wang, M. Asadi, D. Tuschel, J. E. Indacochea, R. F. Klie, A. Salehi-Khojin, *Adv. Mater.* **2015**, *27*, 1887 – 1892.
[14] A. H. Woomer, T. W. Farnsworth, J. Hu, R. A. Wells, C. L. Donley, S. C. Warren, *ACS Nano* **2015**, *9*, 8869 – 8884.
[15] Y. Du, L. Yang, H. Zhou, P. D. Ye, *IEEE Electron Device Lett.* **2016**, *37*, 429 – 432.
[16] D. Yue, D. Lee, Y. D. Jang, M. S. Choi, H. J. Nam, D.-Y. Jung, W. J. Yoo, *Nanoscale* **2016**, *8*, 12773 – 12779.
[17] D. Hanlon et al., *Nat. Commun.* **2015**, *6*, 8563.
[18] C. R. Ryder, J. D. Wood, S. A. Wells, M. C. Hersam, *ACS Nano* **2016**, *10*, 3900 – 3917.
[19] C. R. Ryder, J. D. Wood, S. A. Wells, Y. Yang, D. Jariwala, T. J. Marks, G. C. Schatz, M. C. Hersam, *Nat. Chem.* **2016**, *8*, 597 – 602.
[20] Y. Zhao, H. Wang, H. Huang, Q. Xiao, Y. Xu, Z. Guo, H. Xie, J. Shao, Z. Sun, W. Han, X.-F. Yu, P. Li, P. K. Chu, *Angew. Chem. Int. Ed.* **2016**, *55*, 5003 – 5007; *Angew. Chem.* **2016**, *128*, 5087 – 5091.
[21] T.-C. Tseng et al., *Nat. Chem.* **2010**, *2*, 374 – 379.
[22] M. R. Suchanski, R. P. Van Duyne, *J. Am. Chem. Soc.* **1976**, *98*, 250 – 252.
[23] L. Ballester, A. M. Gil, A. Gutiérrez, M. F. Perpiñán, M. T. Azcondo, A. E. Sánchez, E. Coronado, C. J. Gómez-García, *Inorg. Chem.* **2000**, *39*, 2837 – 2842.
[24] M. R. Saber, A. V. Prosvirin, B. F. Abrahams, R. W. Elliott, R. Robson, K. R. Dunbar, *Chem. Eur. J.* **2014**, *20*, 7593 – 7597.
[25] X. Zhang, M. R. Saber, A. P. Prosvirin, J. H. Reibenspies, L. Sun, M. Ballesteros-Rivas, H. Zhao, K. R. Dunbar, *Inorg. Chem. Front.* **2015**, *2*, 904 – 911.
[26] R. Zhang, B. Li, J. Yang, *J. Phys. Chem. C* **2015**, *119*, 2871 – 2878.
[27] Y. Jing, Q. Tang, P. He, Z. Zhou, P. Shen, *Nanotechnology* **2015**, *26*, 095201.
[28] Y. He, F. Xia, Z. Shao, J. Zhao, J. Jie, *J. Phys. Chem. Lett.* **2015**, *6*, 4701 – 4710.
[29] E. I. Kamitsos, W. M. Risen, Jr., *J. Chem. Phys.* **1983**, *79*, 5808 – 5819.
[30] B. Milián, R. Pou-Amérigo, R. Viruela, E. Ortí, *J. Mol. Struct. (Theochem)* **2004**, *709*, 97 – 102.
[31] R. J. Wu, M. Topsakal, T. Low, M. C. Robbins, N. Haratipour, J. S. Jeong, R. M. Wentzcovitch, S. J. Koester, K. A. Mkhoyan, *J. Vac. Sci. Technol. A* **2015**, *33*, 060604.
[32] C. Backes, C. D. Schmidt, K. Rosenlehner, F. Hauke, J. N. Coleman, A. Hirsch, *Adv. Mater.* **2010**, *22*, 788 – 802.
[33] N. V. Kozhemyakina, J. M. Englert, G. Yang, E. Spiecker, C. D. Schmidt, F. Hauke, A. Hirsch, *Adv. Mater.* **2010**, *22*, 5483 – 5487.
[34] C. Wirtz, T. Hallam, C. P. Cullen, N. C. Berner, M. O'Brien, M. Marcia, A. Hirsch, G. S. Duesberg, *Chem. Commun.* **2015**, *51*, 16553 – 16556.
[35] M. Marcia, P. Singh, F. Hauke, M. Maggini, A. Hirsch, *Org. Biomol. Chem.* **2014**, *12*, 7045.
[36] J. M. Englert, J. Röhrl, C. D. Schmidt, R. Graupner, M. Hundhausen, F. Hauke, A. Hirsch, *Adv. Mater.* **2009**, *21*, 4265 – 4269.

Received: May 16, 2016
Revised: July 17, 2016
Published online: October 20, 2016

